Method for reducing noise in X-ray images by averaging pixels based on the normalized difference with the relevant pixel

**Masayuki Nishiki · Kunio Shiraishi ·
Takuya Sakaguchi · Kyojiro Nambu**

Abstract A real-time digital filter for noise reduction in X-ray images is proposed. The filter is based on averaging of only similar pixels (pixels that differ only little) rather than neighboring pixels, which are averaged in conventional linear low-pass filters. The effectiveness of the filter was evaluated by computer simulation, where original images that were acquired by X-ray exposure were processed in accordance with the filter algorithm. The resulting images were evaluated in terms of the pre-sampled modulation transfer function (MTF), the noise power spectrum (NPS), and the lag. Comparison of the filtered and original images revealed that the NPS was reduced for the full range of spatial frequencies in the filtered image, resulting in a reduction of total noise power to about 1/9 the level in the original image with no degradation in the MTF or lag. The usefulness of the filter was demonstrated in fluoroscopic, digital subtraction angiography (DSA) and mammographic phantom studies. The filter was found to have the potential to reduce the patient dose by reducing the noise in dynamic as well as static X-ray images.

M. Nishiki (✉) · T. Sakaguchi · K. Nambu
Toshiba Medical Systems Corporation,
1385 Shimoishigami, Otawara, Tochigi 324-8550, Japan
e-mail: masayuki.nishiki@toshiba.co.jp

K. Shiraishi
Toshiba Medical Systems Engineering Co., Ltd.,
1385 Shimoishigami, Otawara, Tochigi 324-8550, Japan

M. Nishiki
Division of Radiological Sciences,
International University of Health and Welfare Graduate School,
2600-1 Kita-Kanemaru, Otawara, Tochigi 324-8501, Japan

1 Introduction

X-ray images are inherently associated with noise, which is classified into two categories, quantum and non-quantum noise. Because noise in any form interferes with medical diagnosis, efforts to reduce noise are essential in both existing and future X-ray systems. Although the non-quantum part of the noise in electronic images can be reduced by improvement in the detector electronics, such as the preamplifier to be used for reading electronic signals from detector pixels [1–3], the quantum part of the noise is difficult to reduce because it is inherent in X-ray imaging. A common method used for reducing the effects of quantum noise is to increase the detector exposure. However, this approach causes a corresponding increase in the patient dose. Thus, a method of reducing the effect of quantum noise without increasing the patient dose is required. Such a method can be used for reducing the patient dose, because, with this reduced dose, one can achieve the required image quality.

Various methods [4–12] have been proposed for reducing noise in X-ray imaging. Of these, the simpler methods are based on a linear filter that is composed of a temporal and/or a spatial low-pass filter. Although linear low-pass filters can reduce noise, they also reduce the signal components. The resulting filtered images are generally blurred in the temporal and/or spatial direction(s), depending on the filter(s) applied.

For overcoming the limitations of linear filters, several improvements have been proposed, including a temporal filter combined with motion detection [5], an edge-preserving

adaptive filter [6–8], a non-linear diffusion filter [9], and a median filter or a multi-resolution filter [10, 11]. In the present study, we aim to contribute a new such filter that is free from the limitation of linear filters but still has an adequate noise reduction capability. One of the authors has proposed a useful method, referred to as a coherence filter (CF) [12], for reducing the quantum noise in medical diagnostic images. The noise reduction in the CF is achieved by averaging of only *similar* pixels (pixels that differ only little) instead of spatially and/or temporally neighboring pixels, which are averaged in linear low-pass filters. In the CF, averaging is based on the *difference*, which is calculated by a specific equation, and the averaged pixels are not necessarily located close to each other. Because similar pixels (pixels that differ only little) have similar spatial/temporal characteristics, they can be averaged without affecting the resolution.

In a study referred to above [12], the basic concept of the CF was developed, and two types of CF, a temporal CF and a volumetric CF, were defined. The temporal CF was applied to two-dimensional (2D) dynamic CT study images, whereas the volumetric CF was applied to volumetric CT images. In the present study, the basic concept of CF was extended so that it could be adapted to X-ray imaging, including both high-resolution static imaging (such as mammography) and real-time dynamic imaging (such as fluoroscopy). In static imaging, the filter can be applied directly to a 2D image by use of only the image concerned. In real-time dynamic imaging, multiple images are used when the filter is applied to each image. Because the filtered image has to be displayed immediately after X-ray exposure of the patient, it is not possible to use recorded images for post-processing to achieve filtering as is the case in CT imaging. Therefore, the real-time imaging method proposed in this study uses only the present image and some past images, but no future images.

Thus, our purpose in this study was to extend the basic concept of the CF so that it could be adapted to high-resolution static imaging as well as to real-time dynamic imaging, both of these for X-ray imaging. Furthermore, the pre-sampled modulation transfer function (MTF) and the noise power spectrum (NPS) of the CF were evaluated quantitatively in this study as the basic image quality metrics, which were not evaluated in the previous study [12].

2 Materials and methods

2.1 Coherence filter (CF)

As described above, the noise reduction in the CF is achieved by averaging of only similar pixels (pixels that differ only little) instead of spatially and/or temporally neighboring pixels. To this end, the CF process starts with defining the pixel $\mathbf{x}_k$ with the pixel value $v(\mathbf{x}_k)$, where $\mathbf{x}$ denotes the spatial position vector and k denotes the present time. Then, $d(\mathbf{x}_k, \mathbf{y}_k)$, the normalized difference between two pixels ($\mathbf{x}_k$ and $\mathbf{y}_k$), is defined by the following equation:

$$d(\mathbf{x}_k, \mathbf{y}_k) = \frac{\sqrt{\sum_{t=0}^{l} \sum_{\mathbf{a}} \left(v(\mathbf{x}_{k-t} + \mathbf{a}) - v(\mathbf{y}_{k-t} + \mathbf{a}) \right)^2}}{K\sigma(\mathbf{x}_k)}, \qquad (1)$$

where $\mathbf{a}$ is a spatial vector defined in the image plane, $\sigma(\mathbf{x}_k)$ is the standard deviation of the noise associated with $v(\mathbf{x}_k)$, K is a constant, and t is an index that indicates the relative time, with $t = 0$ corresponding to the present (latest) frame and $t = 1$ corresponding to the immediately preceding frame. Note that, when the CF is applied to static imaging, $l = 0$. The numerator in Eq. 1 is a quantity that represents the difference between the two pixels, which is calculated from the pixel pair ($\mathbf{x}_k$ and $\mathbf{y}_k$) and their neighboring pixels, which are characterized by $\mathbf{a}$ and t. The difference thus derived is normalized against $K\sigma(\mathbf{x}_k)$ to generate $d(\mathbf{x}_k, \mathbf{y}_k)$. This normalization allows $d(\mathbf{x}_k, \mathbf{y}_k)$ values to be compared even when the exposure at the detector changes. While the system setting stays unchanged, $\sigma(\mathbf{x}_k)$ is proportional to $\sqrt{v(\mathbf{x}_k)}$ in image areas where the X-ray quantum noise is dominant. $\sigma(\mathbf{x}_k)$ can include not only the X-ray quantum noise, but also the electronic noise associated with the readout circuit, and it can be tabulated in advance in terms of the pixel value and the system settings such as the gain.

The CF reduces noise by averaging similar pixels (pixels that differ only little). The filtered pixel value $v'(\mathbf{x}_k)$ is given by the following equation:

$$v'(\mathbf{x}_k) = \frac{\sum_{\mathbf{y}_k \in N(\mathbf{x}_k)} v(\mathbf{y}_k) \times w(d(\mathbf{x}_k, \mathbf{y}_k))}{\sum_{\mathbf{y}_k \in N(\mathbf{x}_k)} w(d(\mathbf{x}_k, \mathbf{y}_k))}, \qquad (2)$$

where $N(\mathbf{x}_k)$ is the area containing the pixels to be averaged and $w(d(\mathbf{x}_k, \mathbf{y}_k))$ is the weighting factor for $v(\mathbf{y}_k)$. In general, $w(d(\mathbf{x}_k, \mathbf{y}_k))$ is a monotonically decreasing function of $d(\mathbf{x}_k, \mathbf{y}_k)$, because the weighting factor should be small when the normalized difference between pixels is large. An example of filter implementation is shown in Fig. 1, where $\mathbf{a}$ consists of the nine vectors $[-1, -1]$, $[-1, 0]$, $[-1, 1]$, $[0, -1]$, $[0, 1]$, $[1, -1]$, $[1, 0]$, $[1, 1]$, and $[0, 0]$, $l = 2$, and $N(\mathbf{x}_k)$ contains the $N \times N$ pixels surrounding $\mathbf{x}_k$. In this study, the above 9 vectors were used as $\mathbf{a}$, l was assumed to be 2 for dynamic imaging and 0 for static imaging, and N was assumed to be 11. The principles of the CF do not require $N(\mathbf{x}_k)$ to be the surrounding pixels of $\mathbf{x}_k$, but based on practical implementation considerations, the surrounding pixels were used as $N(\mathbf{x}_k)$ in this study. Also, $w(d(\mathbf{x}_k, \mathbf{y}_k))$ is determined only by the normalized difference between $\mathbf{x}_k$ and $\mathbf{y}_k$ and not by the physical distance between $\mathbf{x}_k$ and $\mathbf{y}_k$.
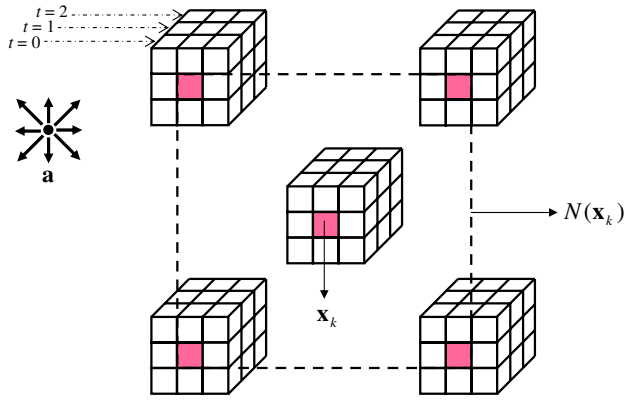
Fig. 1 Example of CF implementation. In this study, a set of $3 \times 3 \times 3 = 27$ pixels was used in the calculation of the normalized difference, and the 11×11 pixels surrounding $\mathbf{x}_k$ were chosen as $N(\mathbf{x}_k)$

Fig. 2 Example of the weighting factor. Generally, a monotonically decreasing function of the normalized difference is used

In addition, $w(d(\mathbf{x}_k, \mathbf{y}_k))$ can be any type of monotonically decreasing function of $d(\mathbf{x}_k, \mathbf{y}_k)$, depending on the nature of the images to be processed. One example of $w(d(\mathbf{x}_k, \mathbf{y}_k))$ is shown in Fig. 2 which has the shape of $\{1 - (\text{cumulative distribution function of the normal distribution})\}$. This particular shape was selected because $d(\mathbf{x}_k, \mathbf{y}_k)$ approximately obeys the normal distribution when there is only noise in the image. We applied this shape of $w(d(\mathbf{x}_k, \mathbf{y}_k))$ to obtain the results in this study.
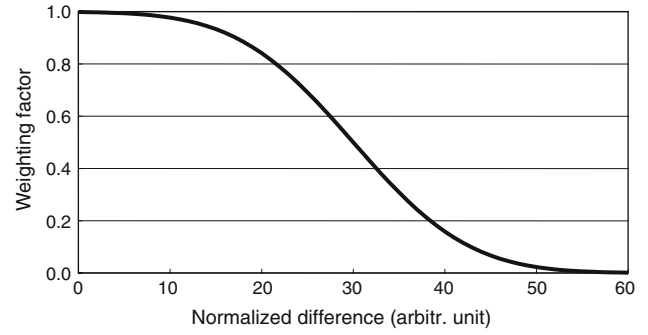
2.2 Experimental setup

X-rays were generated with use of a Toshiba XTP-8100G generator connected to a Toshiba DRX-T7445GFS tube, and the Toshiba Flat Panel Detector (FPD) XIDF-FPD801 (0.194-mm pixel pitch) was used as the X-ray detector throughout this study unless stated otherwise. $\sigma(\mathbf{x}_k)$ was pre-measured in terms of the pixel value and the system settings such as the gain, and was tabulated in advance.

2.3 Modulation transfer function

The MTF was measured by use of the slanted edge technique [13, 14]. An edge of a 1-mm-thick tungsten plate was placed on the detector surface without an anti-scatter grid or phantom. The beam quality was adjusted to RQA5 [15] with a tube voltage of 70 kVp. Only the MTF in the vertical direction (signal-line direction of the FPD) was measured. The integer number of lines (rows) that leads to an approximately 1-pixel shift of the edge was determined to be 48. The sampling distance of the oversampled edge spread function was assumed to be constant, in accordance with reference [16].

The edge images were acquired only for the original images, and these images were used for computer simulation of the edge images for the CF images. Thus, exactly the same slant angle was applied to both types of images. No interpolation was applied to the images; as a result, the pixel pitch in each image was 0.194 mm. Three original images were employed ($l = 2$) for generating 1 CF image with use of Eqs. 1 and 2.

2.4 Noise power spectrum

The NPS for the original images was calculated from an X-ray image with uniform exposure that was acquired with RQA5 beam quality. The CF image was computer-simulated by use of these original images ($l = 2$). No interpolation was applied to the image, as in the MTF measurement described above. The NPS for the CF image was calculated from the above computer-simulated CF image. The exposure at the detector was 1 μGy (115 μR). First, the full image of $1,024 \times 1,024$ pixels was divided into 36 subregions of 128×128 pixels each. These subregions overlapped each other by 64 pixels each in the horizontal and vertical directions. The square of the modulus of the 2D Fourier transform for each subregion was calculated and divided by 128^2 and the (pixel value)^2, and then multiplied by the area of a pixel (0.0376 mm^2). Next, we obtained the average over all 36 subregions in order to determine the final 2D NPS. The calculation of the NPS here conformed exactly with reference [17]. The resultant NPS corresponds to the normalized NPS in reference [17]. The 1D NPS in the vertical direction (signal line direction of the FPD) was extracted from the 2D NPS by use of one line just next to the central axis.

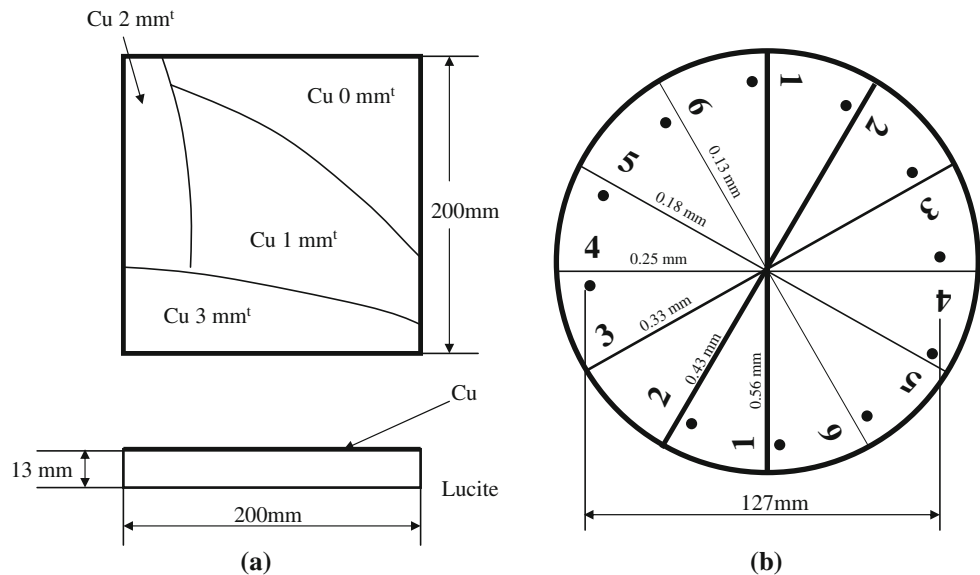### 2.5 Experimental setup for phantom images

First, the CF was applied to fluoroscopic images. Original fluoroscopic images were acquired with the setup shown in Fig. 3, whereas filtered images were computer-simulated from the original images. The original images were

acquired with the X-ray conditions of 80 kVp, 116 mA, 9.93 ms pulse width, and 15 frames/s. The X-rays from the source passed through a 0.06-mm Ta filter, a patient table, phantoms, and an anti-scatter grid before reaching the detector. The patient table is made of carbon fiber as in a standard angiographic C-arm system. The phantoms included a 150-mm-thick Lucite phantom, a cardiovascular (CV) phantom, and two spoke test disks (disk 1 rotated at 30 rpm, while disk 2 was stationary), as shown in Fig. 4. The CV phantom in Fig. 4a simulates the human heart area by using copper sheets of different thickness, whereas each spoke test disk (Nuclear Associates, model 07-629) contains six steel music wires of diameters 0.56, 0.43, 0.33, 0.25, 0.18, and 0.13 mm as shown in Fig. 4b. The phantom images that were used in the evaluation of fluoroscopic images were acquired with a field of view (FOV) of 7 in.,
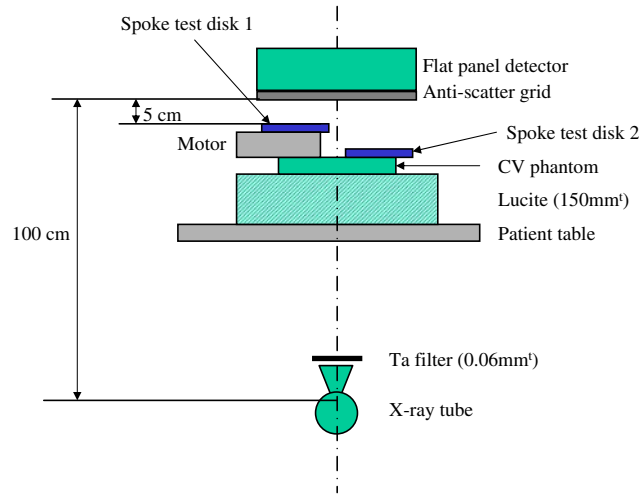
whereas the full FOV of the detector was 8 in. A 7-in. FOV was selected because it is widely used in cardiac applications. The effective pixel size was thus reduced from the original size of 0.194 mm to $0.194 \times 7/8 = 0.170$ mm.
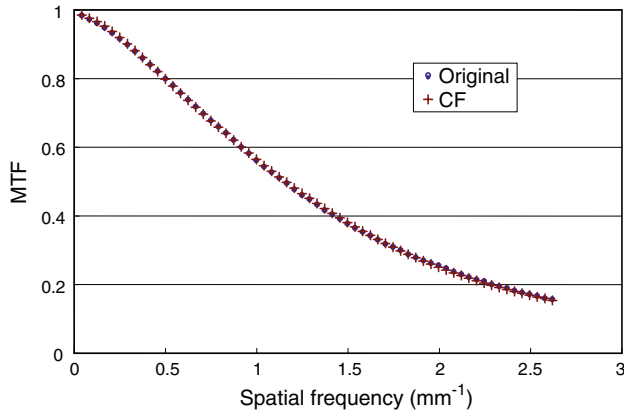
The CF was also applied to digital subtraction angiography (DSA) images that were acquired in accordance with the IEC standard 61223-3-3:1996 [18]. The same CF parameters as used for the fluoroscopic images were applied, except for $\sigma(\mathbf{x}_k)$, which depends on the exposure. Because DSA images were acquired in a sequence as in normal clinical situations, it was possible to set the parameter l to be 2. The detector pixel pitch was 0.170 mm, as for fluoroscopic imaging. The exposure at the detector was 2.17 μGy (248 μR) with a tube voltage of 75 kVp.

Finally, the CF was applied with $l = 0$ to a static image of the ACR (American college of radiology)-specified model 156 phantom that is widely used for mammographic imaging. The original image was acquired with use of Toshiba DRX-B3856HED-Mo as the X-ray tube and Toshiba TFP-2400A as the detector (0.085-mm pixel pitch). No interpolation was applied to the image. The exposure at the detector was 70 μGy (8 mR) with a tube voltage of 28 kVp. The target material and the X-ray filter were both Mo.

3 Results

3.1 MTF measurement

The MTF measurement results are shown in Fig. 5 for the original image and the CF image. Because the detector output was observed to be proportional to the input

Fig. 3 Experimental setup for fluoroscopic image acquisition

Fig. 4 Details of the phantoms used in the experimental setup. **a** Cardiovascular (CV) phantom, which simulates the human heart with use of copper sheets of different thickness. **b** Spoke test disk, which consists of six steel music wires of different diameters

Fig. 5 The MTF of an original image and the corresponding CF image in the vertical direction. The two MTF curves overlap closely, indicating that the CF does not cause any blurring

Fig. 6 The NPS of an original image and the corresponding CF image in the vertical direction at an exposure of 1 μGy (115 μR). The total noise power in the CF image was reduced to about 1/9 the level in the original image

exposure (not shown), no special linearization process was applied to the image data. The two MTF curves overlapped closely, indicating that, in contrast to conventional spatial low-pass filtering, the CF caused no blurring.

3.2 NPS measurement

The NPS measurement results are shown in Fig. 6. Because the detector output was observed to be proportional to the input exposure (not shown), no special linearization process was applied to the image data. Although the CF reduces noise throughout the frequency range, the noise reduction is greater at higher frequencies (around 2.0 mm^{-1}). The total noise power (noise variance) was evaluated by integration of the NPS curve through the whole frequency range, and was found to be reduced to about 1/9 the level in the original image.
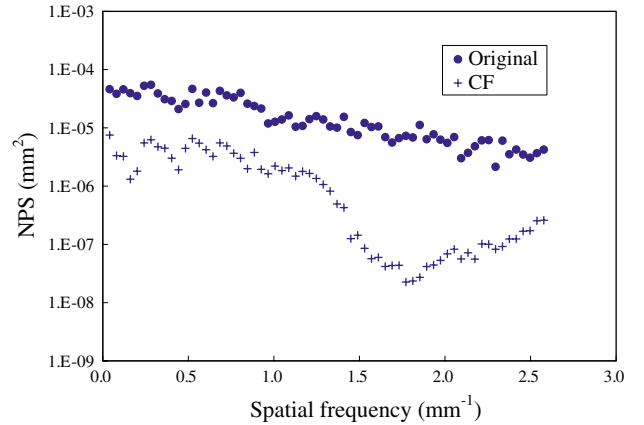
3.3 Phantom images

The results for fluoroscopic images are shown in Fig. 7. The original image in Fig. 7a was acquired with the setup shown in Fig. 3, whereas the filtered images in Fig. 7b and c were computer-simulated from the original images. The exposure in the center area (superimposed square) was 52 nGy (6 μR). The CF image was generated with the parameters described in Sect. 2, and the temporal filter image was generated by use of the following recursive equation:

$$v'(\mathbf{x}_k) = i \times v(\mathbf{x}_k) + (1 - i) \times v'(\mathbf{x}_{k-1}), \tag{3}$$

where i is a constant that is set to 0.7 in Fig. 7c.

The images of the center square areas in Fig. 7a–c are magnified in Fig. 7d–f, respectively, to facilitate image comparison. The noise in the CF image is reduced significantly relative to the original image, with no blurring of

stationary or moving objects. The noise in the temporal filter image is also reduced, but with significant blurring in the moving object.

The result for a DSA image is shown in Fig. 8, and that for the ACR-specified model 156 phantom is shown in Fig. 9. In both cases, the noise was greatly reduced without any significant degradation in spatial resolution.

4 Discussion

Through computer simulations, we have quantitatively investigated the performance of the CF in terms of the MTF and the NPS, and we confirmed that the CF substantially reduces image noise without sacrificing spatial resolution. These features are expected to be extremely useful in interventional procedures, where it is necessary to depict guidewires/catheters clearly while maintaining a low patient dose. The improved visualization of devices and vessels resulting from the use of the CF in interventional procedures may reduce the total X-ray exposure time, leading to reduction of the patient dose even if the exposure per X-ray pulse remains unchanged. Alternatively, the exposure per X-ray pulse could be reduced to give the same image quality as for images without the CF, leading to reduction of the patient dose even if the X-ray exposure time is not reduced. Thus, the CF could contribute to patient dose reduction by combining both effects described above. The issue of how best to exploit the reduction in noise produced by the CF in terms of patient dose reduction by finding the best combination of both effects will be studied in detail in the future.

In addition to the MTF and the NPS characteristics of the CF, we have shown through fluoroscopic image observations that the CF does not introduce any lag or other

Fig. 7 Fluoroscopic images. **a** Original image. **b** CF image. **c** Temporal filter image. Magnified views of the center square area in (**a**), (**b**), and (**c**), respectively. **d** Original image. **e** CF image. **f** Temporal filter image

(a) Original image

(b) CF image

(c) Temporal filter image

(d) Original image (magnified)

**(e)** CF image (magnified)

(f) Temporal filter image (magnified)
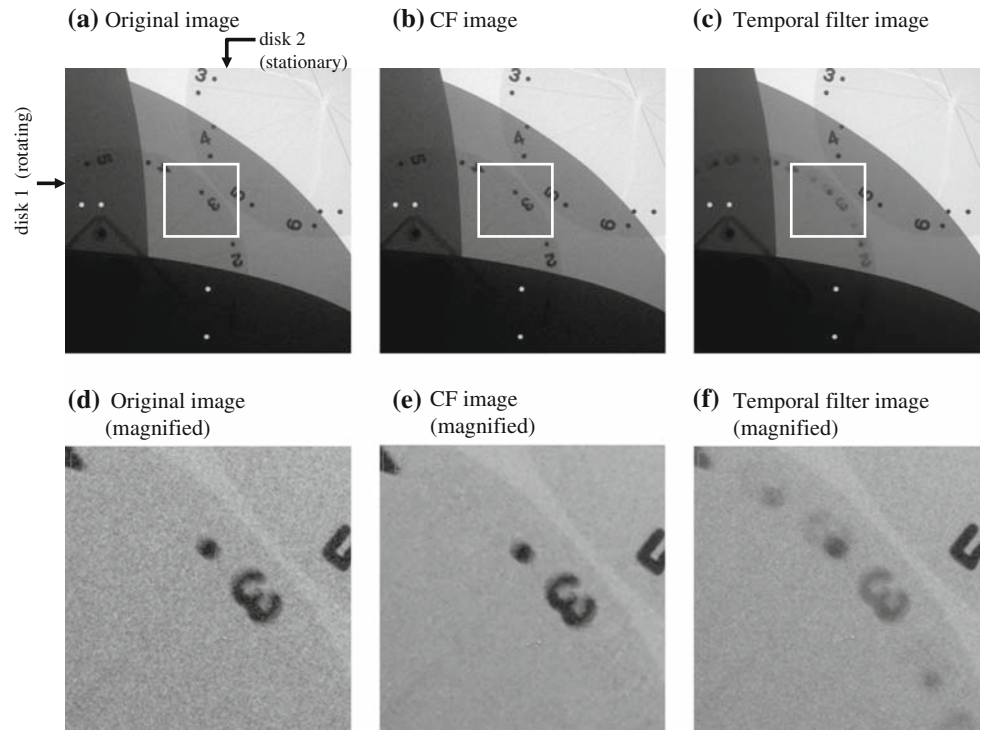
Fig. 8 DSA phantom images and DSA phantom. **a** Original image acquired in accordance with IEC standard 61223-3-3:1996. **b** CF image computer-simulated from the original image. **c** DSA phantom. Because the thickness of the DSA phantom increases stepwise from left to right as shown in (**c**), noise increases from the left to the right ends of the images

(a) Original image

(b) CF image

(c) DSA phantom

Cu

Lucite
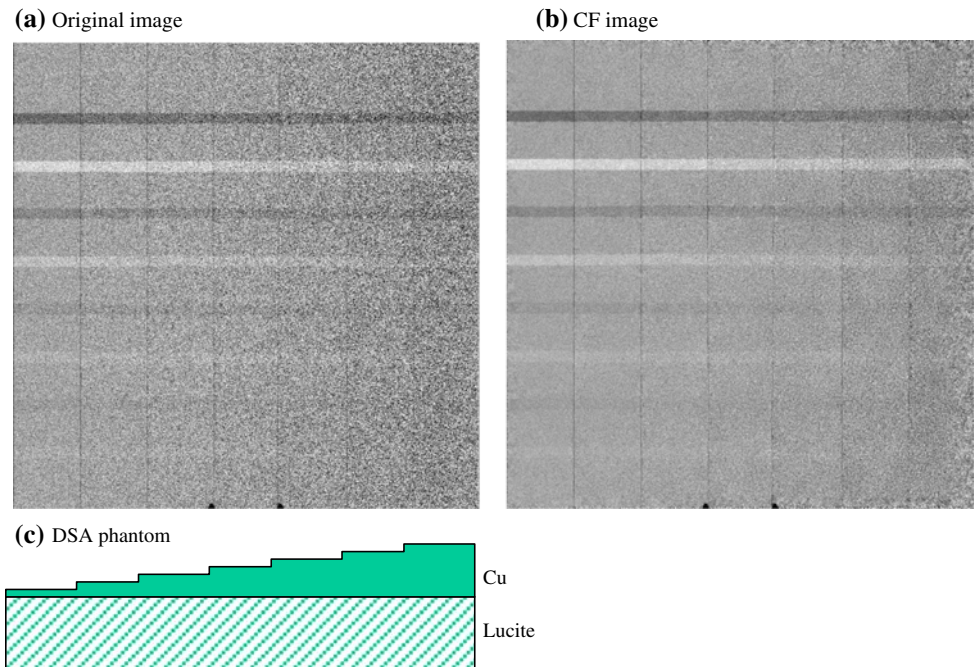
artifacts. Lag in digital image processing is generally caused by any kind of temporal averaging. Because the pixel averaging adopted in the CF is limited within the present image, there is no temporal averaging in the CF. This could be the main reason why there is no lag introduced into the CF images.

We have demonstrated through a qualitative phantom study that the CF can be applied effectively to DSA sequential (dynamic) images by use of the same parameters as are used for fluoroscopy, even though the exposure at the detector surface in DSA is about 40 times greater than that for fluoroscopy. Normalization against $\sigma(\mathbf{x}_k)$ in Eq. 1

Fig. 9 ACR-specified model 156 phantom images. **a** Original image. **b** CF image computer-simulated from the original image
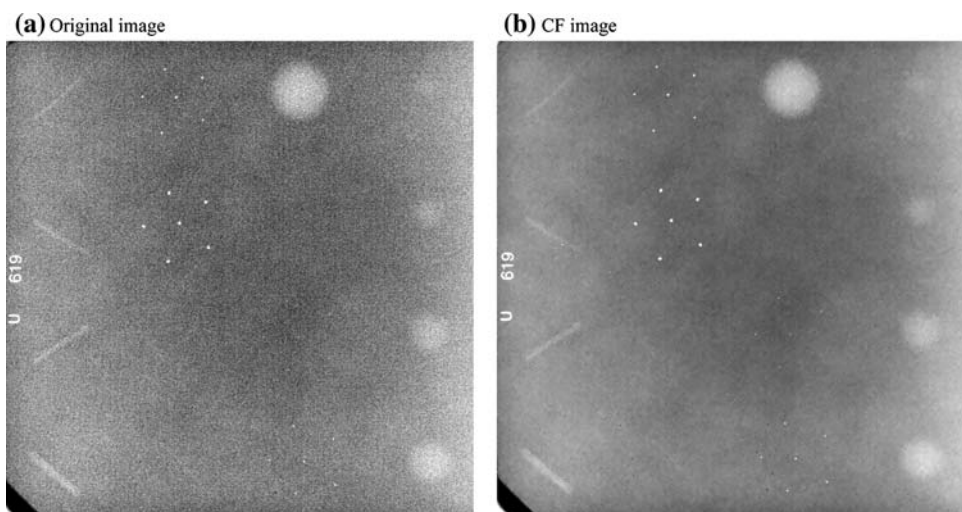
enables the CF to be used effectively for images with very different exposure characteristics, such as fluoroscopic images and DSA images.

We have also demonstrated that the CF has the potential for application to static images, where $l = 0$. Although setting l equal to 0 could reduce the accuracy of the difference calculations, the resulting CF phantom image in Fig. 9 demonstrates a substantial noise reduction without any significant loss of spatial resolution.

We have shown that the NPS in the CF images is reduced more in higher-frequency regions (≥ 1.5 mm^{-1}) than in lower-frequency regions. This could be explained by the fact that, in Eq. 1, we adopted the vector **a** that runs within the 3×3 pixel region. When this **a** is used, noise components for frequencies below that corresponding to a 3-pixel long distance (0.194 mm $\times$ 3 = 0.582 mm), that is, 1.7 mm^{-1}, are not well recognized as the difference according to Eq. 1. Thus, the lower-frequency noise components below 1.7 mm^{-1} were not reduced well in the present study. Optimization of the CF in terms of the frequency response will be undertaken in the future, taking the point of view of practical implementation into account. This imperfect frequency response could be a possible limitation of the CF.

5 Conclusion

The performance of the CF was evaluated in terms of the pre-sampled MTF, NPS, and phantom images. The MTF evaluation demonstrated that the CF did not introduce blurring into filtered images, whereas the NPS evaluation showed that the CF could reduce image noise over the full frequency range, with the total noise power reduced to about 1/9 the level in the original images. The observation of phantom images also indicated that the CF does not

introduce any lag or other artifacts into dynamic imaging. In addition, the CF was shown to be effective for static as well as dynamic images. Thus, the CF can be applied to all types of X-ray images for reducing the image noise and consequently reducing the patient dose.

References

1. Maolinbay M, El-Mohri Y, Antonuk LE, Jee K-W, Nassif S, Rong X, et al. Additive noise properties of active matrix flat-panel imagers. Med Phys. 2000;27:1841–54.
2. El-Mohri Y, Antonuk LE, Zhao Q, Maolinbay M, Rong X, Jee K-W, et al. A quantitative investigation of additive noise reduction for active matrix flat-panel imagers using compensation lines. Med Phys. 2000;27:1855–64.
3. Zhao W, Rowlands JA. X-ray imaging using amorphous selenium: feasibility of a flat panel self-scanned detector for digital radiology. Med Phys. 1995;22:1595–604.
4. Barrett HH, Swindell W. Radiological imaging. New York: Academic; 1981. p. 29–61.
5. Jaffe CC, Orphanoudakis SC, Ablow RC. The effect of a television digital noise reduction device on fluoroscopic image quality and dose rate. Radiology. 1982;144:789–92.
6. Funama Y, Awai K, Miyazaki O, Nakayama Y, Goto T, Omi Y, et al. Improvement of low-contrast detectability in low-dose hepatic multidetector computed tomography using a novel adaptive filter: evaluation with a computer-simulated liver including tumors. Invest Radiol. 2006;41:1–7.
7. Sasaki T, Hanari T, Sasaki M, Oikawa H, Gakumazawa H, Okumura M, et al. Reduction of radiation exposure in CT perfusion study using a quantum de-noising filter. Jpn J Radiol Technol. 2004;60:1688–93 [in Japanese].

8. Honda M, Shiraishi K. An image processing method for fluoroscopy using a linear shadow detection. Med Imaging and Inf Sci. 2004;21:239–51 [in Japanese].

9. Saito N, Kudo K, Sasaki T, Uesugi M, Koshino K, Miyamoto M, et al. Realization of reliable cerebral-blood-flow maps from low-dose CT perfusion images by statistical noise reduction using nonlinear diffusion filtering. Radiol Phys Technol. 2008;1:62–74.

10. Vuylsteke P, Dewaele P. Method and apparatus for noise reduction. US Patent 5,461,655;1995.

11. Yamada S, Murase K. Effectiveness of flexible noise control image processing for digital portal images using computed radiography. Br J Radiol. 2005;78:519–27.

12. Nambu K, Iseki H. A noise reduction method based on a statistical test of high dimensional pixel vectors for dynamic and volumetric images. Riv Neuroradiol. 2005;18:21–33.

13. Samei E, Flynn MJ, Reimann DA. A method for measuring the presampled MTF of digital radiographic systems using an edge test device. Med Phys. 1998;25:102–13.

14. Greer PB, Doorm TV. Evaluation of an algorithm for the assessment of the MTF using an edge method. Med Phys. 2000;27:2048–59.

15. Medical diagnostic X-ray equipment—radiation conditions for use in the determination of characteristics. IEC Standard 61267;1994.

16. Medical electrical equipment—characteristics of digital X-ray imaging devices—part 1: Determination of the detective quantum efficiency. IEC Standard 62220-1;2003.

17. Dobbins III JT. Image quality metrics for digital systems. In: Beutel J, Kundel HL, Van Meter RL, editors. Handbook of medical imaging. Vol. 1: SPIE Press; 2000. p. 161–222.

18. Evaluation and routine testing in medical imaging departments—part 3-3: acceptance tests—imaging performance of X-ray equipment for digital subtraction angiography (DSA). IEC Standard 61223-3-3;1996.